AGU PUBLICATIONS

Journal of Geophysical Research: Solid Earth

Supporting Information for

Theoretical and experimental analyses of temperature responses of water-saturated rocks to changes in confining pressure

Xiaoqiu Yang[1, 2], Weiren Lin[3], Hehua Xu[1, 2], Osamu Tadai[4], Xin Zeng[1, 2]

[1]Key Laboratory of Ocean and Marginal Sea Geology, South China Sea Institute of Oceanology, Innovation Academy of South China Sea Ecology and Environmental Engineering, Chinese Academy of Sciences, Guangzhou 511458, China

[2]Southern Marine Science and Engineering Guangdong Laboratory (Guangzhou), Guangzhou 511458, China

[3]Graduate School of Engineering, Kyoto University, Kyoto 615-8540, Japan

[4]Marine Works Japan Ltd., Nankoku 783-8502, Japan

Corresponding author:

Xiaoqiu Yang (yxq2081@scsio.ac.cn), ORCID ID: 0000-0002-3113-8796

Contents of this file

Additional Supporting Information Files uploaded separately

Introduction

This supporting file provides the Figures S1, S2, S3 and S4, Tables S1, S2, S3 and S4, Movies S1, S2 and S3, Brief review of the theory of thermo-poroelasticity, Detailed descriptions about the measurement system, Detailed descriptions about the experimental procedure, and Thermal Equilibrium between the skeletal framework and the pore fluid.

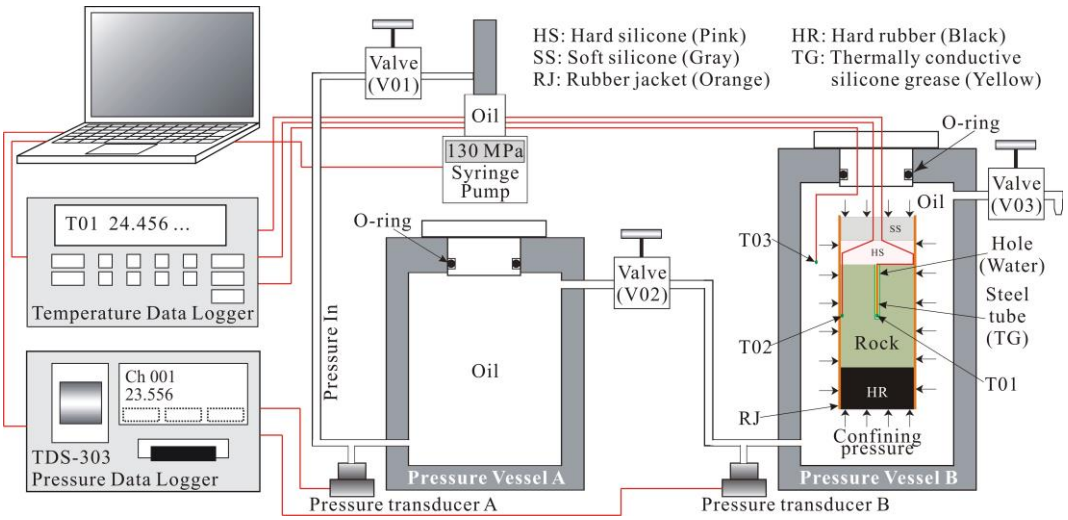

Figure S1. Schematic diagram of the new hydrostatic compression system improved from *Yang et al.* [2017] and used in this study for measuring the adiabatic pressure derivative of the temperature for water-saturated rock specimens (β_{wet}). The system consists of two pressure vessels with a servo-controlled pump that provides pressure up to 130 MPa. The sample assembly is placed in Pressure Vessel B. Three temperature sensors (T01 in sample center, T02 on sample surface and T03 in oil around the rock specimen in the Pressure Vessel B) were deployed for monitoring temperature changes during rapid loading/unloading processes, along with a temperature data logger and a confining pressure data logger.

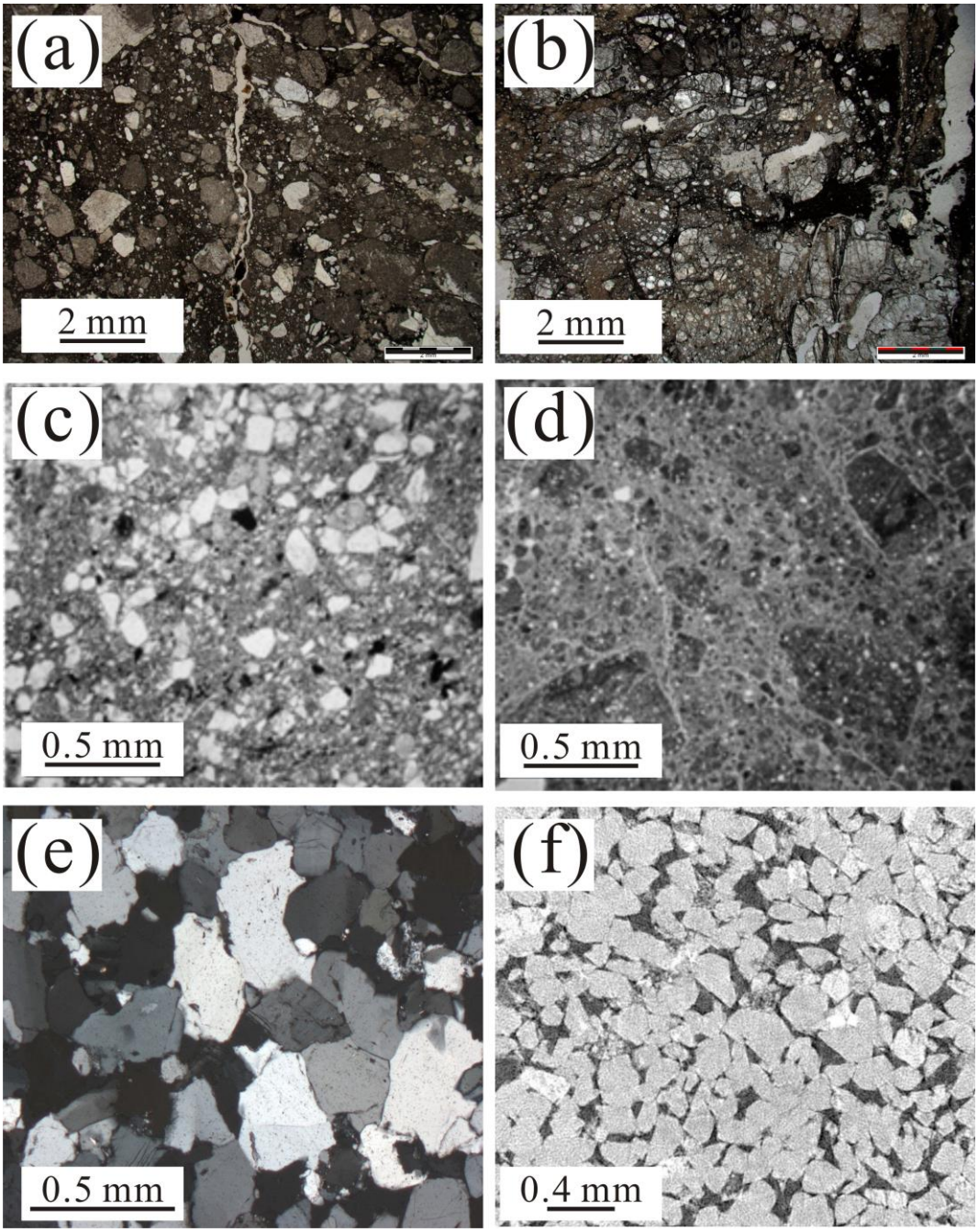

Figure S2. (a-b) Photomicrographs of thin sections (in polarized light) of cataclasite and fault breccia from the Longmenshan Fault Zone [*Wang et al.*, 2014]. (c-d) Photomicrographs of thin sections of fault breccia and gouge from the Chelungpu Fault Zone [*Hashimoto et al.*, 2007]. (e) Photomicrograph of thin section (in crossed polarized light, i.e., under crossed nicol) of Rajasthan sandstone (RJS) from India (provided by Takehiro Hirose). (f) Cross-section of micro-CT image of Berea sandstone (BRS) from the U. S. [*Dong*, 2008].

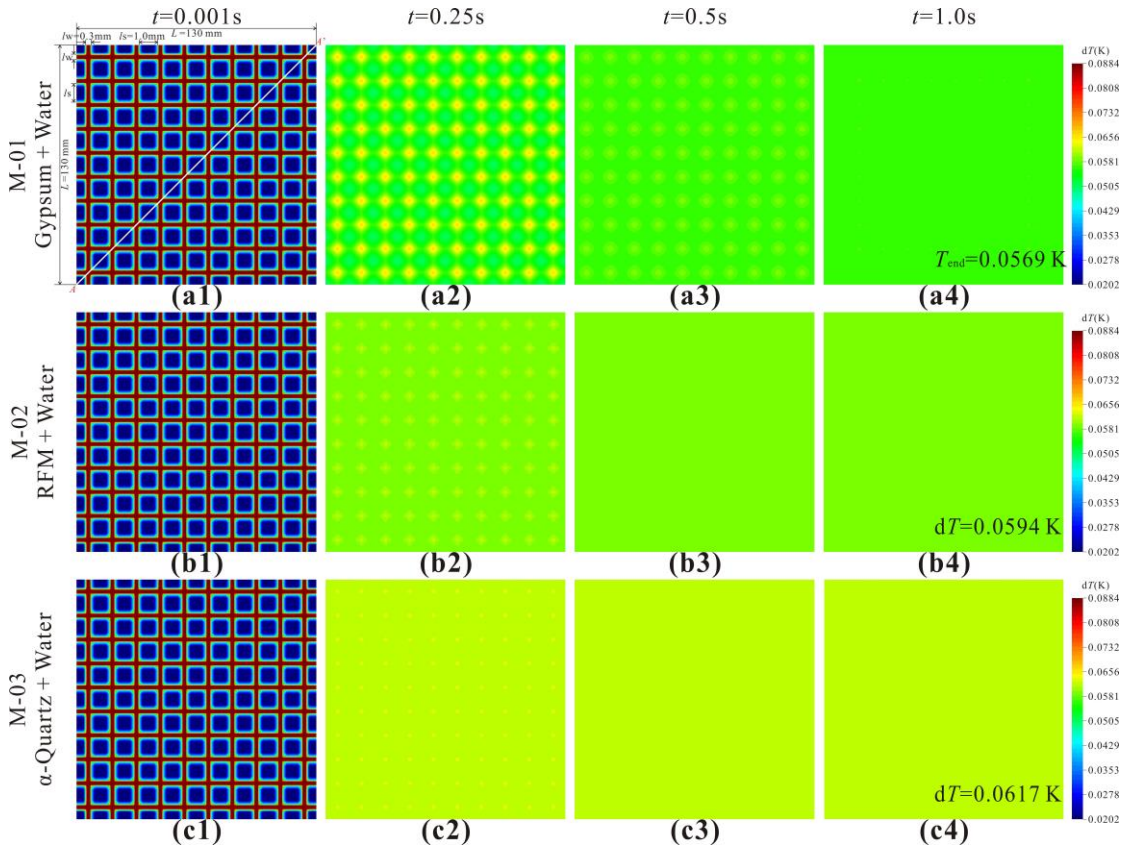

Figure S3. Temperature evolution characteristics of water-saturated rocks with different minerals after instantaneous loading from 0 MPa to 10 MPa (i.e., ΔP_c = 10 MPa). In models M-01, -02 and -03, the solid grains were gypsum (κ_{Gypsum} = 0.51 mm^2/s), main rock-forming minerals averaged (RFM, κ_{RFM} = 2.08 mm^2/s) and α-quartz ($\kappa_{\alpha\text{-quartz}}$ = 4.15 mm^2/s), respectively. In these models, each solid grain is surrounded by pore water, and the equivalent porosity is up to 0.408 (i.e., ϕ = 0.408) since the sizes of grains and pores are set to be 1.0 mm and 0.3 mm, respectively. Each model meshed to 11025 quadrilateral elements with the spatial resolution of 0.2 mm for grains and 0.06 mm for pores, respectively. The time resolution is up to dt = 0.001 s. (a1-a4) Temperature distribution in model M-01 at t = 0.001 s, 0.25 s, 0.5 s and 1.0 s, respectively. (b1-b4) Temperature distribution in model M-02 at t = 0.001 s, 0.25 s, 0.5 s and 1.0 s, respectively. (c1-c4) Temperature distribution in model M-03 at t = 0.001 s, 0.25 s, 0.5 s and 1.0 s, respectively. The temperature profiles along line *A*-*A*' in the three models at t = 0.001 s, 0.25 s, 0.5 s, 0.75 s and 1.0 s, are illustrated in Figure S4.

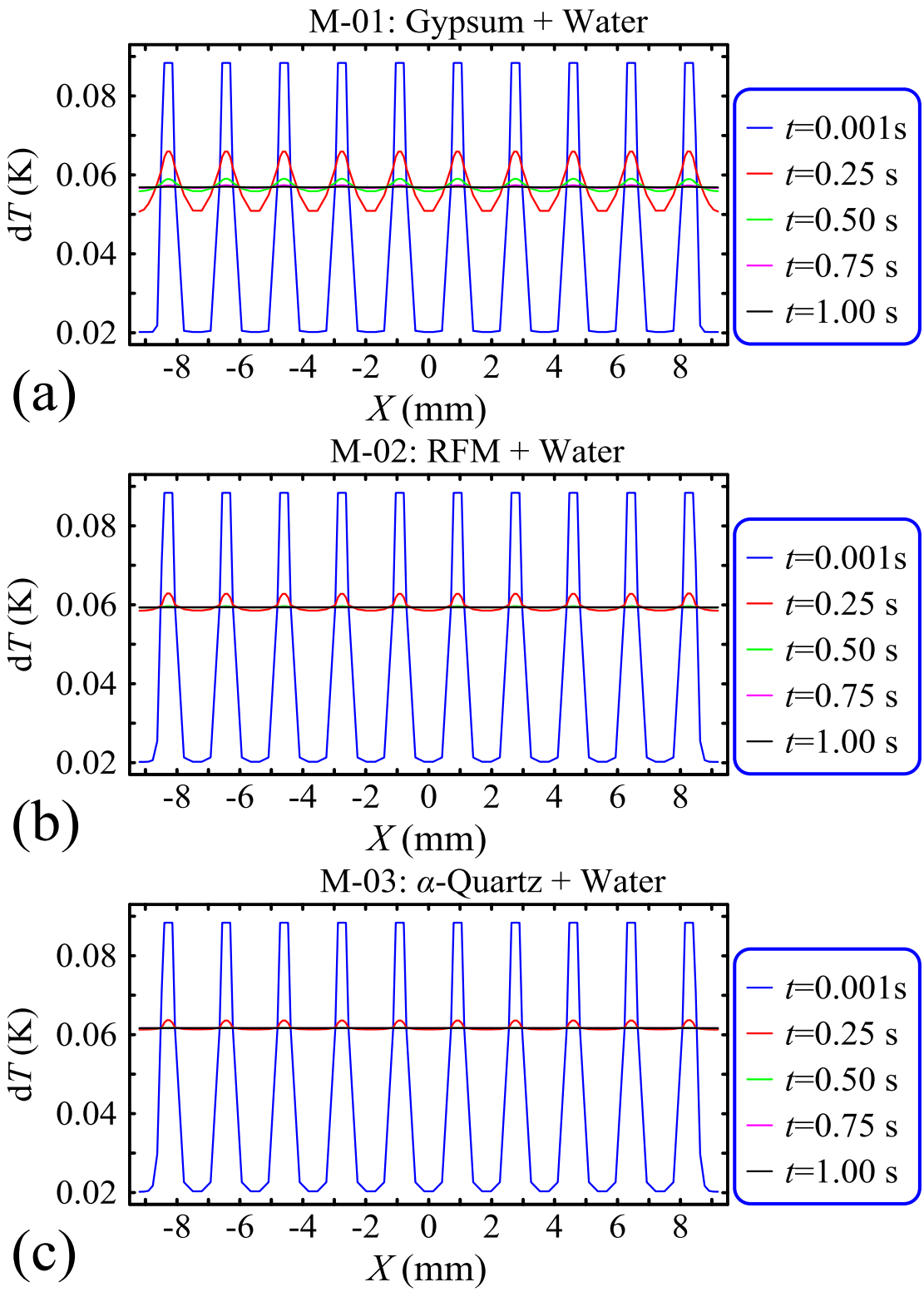

Figure S4. Temperature profiles along the line *A*-*A*' (Figure S3a1) at moment *t*=0.001 s, 0.25 s, 0.5 s, 0.75 s and 1.0 s. In models M-01, -02 and -03, the solid grains were gypsum (κ_{Gypsum} = 0.51 mm^2/s), main rock-forming minerals averaged (RFM, κ_{RFM} = 2.08 mm^2/s) and α-quartz ($\kappa_{\alpha\text{-quartz}}$ = 4.15 mm^2/s), respectively.

Table S3. Estimations of Characteristic Distance for Several Main Rock-Forming Minerals in the crust and Water

Mineral/Material	(ρc)	λ	κ	l (τ'=1 s)	References
	(MJ/(m^3·K))	(W/(m·K))	(mm^2/s)	(mm)	
Feldspar (mean value)	1.740	2.30	1.32	1.149	[*Pan*, 1993; *Schön*, 2011]
α-Quartz	1.854	7.69	4.15	2.037	
Mica (muscovite)	2.152	2.30	1.07	1.034	
Amphibole	2.310	2.90	1.26	1.122	
Pyroxene (enstatite)	2.407	4.47	1.86	1.364	
Pyroxene (diopside)	2.196	4.66	2.12	1.456	
Olivine (forsterite)	2.185	5.03	2.30	1.517	
Calcite	2.168	3.59	1.66	1.288	
Main RFMs (averaged)	2.131	4.01	2.08	1.442	
Gypsum	2.466	1.26	0.51	0.714	
Water (at 25°C and 0.1 MPa)	4.169	0.61	0.15	0.387	[*Lide*, 2010]

Note: 1) λ, κ, and (ρc) are thermal conductivity, thermal diffusivity, and volumetric heat capacity, respectively; 2) l (τ'=1 s) is the characteristic distance when the time interval τ' is 1 s; 3) Main RFMs refers to the main rock-forming minerals.

Table S4. Model Parameters of Numerical Simulations on Thermal Equilibrium between Skeletal Framework and pore water

Model	Material	B	α	ΔP_c (MPa)	ΔP_f (MPa)	ΔP^{eff} (MPa)	β_w (mK/MPa)	β_{frm} (mK/MPa)	A_w (W/m^3)	A_{frm} (W/m^3)	T_{end} (K)
M-01	Gypsum+Water	0.5	0.9506	10.0	5.0	5.247	17.68	3.85	368.435	12.330	0.0569
M-02	RFM+Water	0.5	0.9506	10.0	5.0	5.247	17.68	3.85	368.435	10.655	0.0594
M-03	Quartz+Water	0.5	0.9506	10.0	5.0	5.247	17.68	3.85	368.435	9.270	0.0617

Note: here, the Skempton's coefficient is considered to $B = 0.5$. The effective stress coefficient α was estimated from the porosity (ϕ=0.408) by equation (28). The changes in pore pressure (ΔP_f) and effective pressure (ΔP^{eff}) was calculated with equation (9). The β of the skeletal framework (β_{frm}) was to be 3.85 mK/MPa, which is the mean value of β of dry rocks [*Yang et al.*, 2017]. A_w and A_{frm} are the "heat sources" in pore water and skeletal framework calculated by equation (S8) since the loading was considered to be finished within 0.001 s. T_{end} is the final balance temperature calculated by theoretical equations (9)-(13).

A brief review of the theory of thermo-poroelasticity

In thermoelasticity in general, the mechanical interaction term in the temperature-distribution equation is neglected. In fact, many years ago, *Duhamel* [1837] and *Neumann* [1885] tried to include such an interaction with the argument (for an isotropic substance) that the rate of temperature change was linearly dependent not only on the net rate of heat inflow but also on the rate of dilatation. A detailed discussion of the complete temperature-distribution equation is given by *Biot* [1956]. His equation can be written as

$$\frac{\partial T}{\partial t} = \kappa \frac{\partial^2 T}{\partial t^2} + \frac{K \cdot \alpha_v}{c} \frac{\partial e}{\partial t}, \qquad \text{(S1)}$$

in which, T is temperature, t is time, e is dilatation; κ and c are thermal diffusivity and specific heat, respectively; K and a_v are rock bulk modulus and coefficient of volumetric thermal expansion, respectively. *Lessen* [1956] derived the same equation for a thermoelastic solid from thermodynamical principles. The usual treatment of infinitesimal deformation thermoelastic problems considers the following relations:

Equilibrium: $\rho \frac{\partial^2 u_i}{\partial t} = \sigma_{ki,k} + F_i, \qquad \text{(S2)}$

Generalized Stress-Strain-Temperature Law: $\varepsilon_{ij} = G_{ij,kl}\sigma_{kl} + \alpha_{ij}(T - T_0), \qquad \text{(S3)}$

where u_i is displacement, F_i is body force per unit mass; σ_{ij} and ε_{ij} are stress tensor and strain tensor, respectively; ρ, G_{ijkl} and α_{ij} are density, isothermal elasticity tensor and thermal expansion coefficient tensor, respectively; T and t are temperature and time, respectively. The physical implications of the foregoing ensemble of equations (S1)—(S3) are that, there are not only a thermodynamic interaction term in the generalized stress-strain-temperature law, but also the intuitively expected mechanical interaction term in the temperature-distribution equation [*Lessen*, 1956].

Geertsma [1957a] derived the theory about the effect of fluid pressure decline on volumetric changes of porous rocks and mentioned the thermoelasticity and the elasticity of saturated porous media [*Geertsma*, 1957b], but only discussed the analogous behaviour of the temperature distribution in thermoelastic problems and the liquid pressure distribution in a saturated porous medium [*Geertsma*, 1957b] based on the complete pore pressure-distribution equation [*Biot*, 1941]

$$\frac{1}{Q}\frac{\partial p}{\partial t} = \beta \frac{\partial^2 p}{\partial t^2} - \alpha \frac{\partial e}{\partial t}, \qquad \text{(S4)}$$

which is in structure identical with the complete temperature-distribution equation (S1).

In Equation (S4), p is pore pressure, t is time, e is dilatation, Q and a are not simple measurable physical quantities as in the corresponding temperature-distribution equation (S1). *Norris* [1992] discussed the correspondence between poroelasticity and thermoelasticity too. He found that an interesting and useful analogy can be drawn between the equations of static poroelasticity and the equations of thermoelasticity including entropy. The correspondence is of practical use in determining the effective parameters in an inhomogeneous poroelastic medium using known results from the literature on the effective thermal expansion coefficient and the effective heat capacity of a disordered thermoelastic continuum.

Zimmerman [2000] also briefly derived the equations of linearised poroelasticity and thermoelasticity. His derivation results are the same as the complete pore pressure-distribution equation (S4) [*Biot*, 1941] and the complete temperature-distribution equation (S1) [*Biot*, 1956], respectively. Based on these equations, he presented the dimensionless parameters that quantify the strength of the coupling between mechanical and hydraulic (or thermal) effects. The results show that the poroelastic coupling parameter is shown to be the product of the Biot coefficient and the Skempton coefficient; the thermoelastic coupling parameter can be interpreted as the ratio of stored elastic strain energy to stored thermal energy. For liquid-saturated rocks, the poroelastic coupling parameter usually lies between 0.1 and 1.0, which means that the mechanical deformation has a strong influence on the pore pressure. The thermoelastic coupling parameter is usually very small, so that, although the temperature field influences the stresses and strains, the stresses and strains do not appreciably influence the temperature field.

McTigue [1986, 1990] given the constitutive equations of the linear theory of thermos-poroelasticity as

$$\begin{cases} \varepsilon_{ij} = \frac{1}{2G}\left[\sigma_{ij} - \frac{1}{1+v}\sigma_{ij}\delta_{ij}\right] + \frac{\alpha(1-2v)}{2G(1+v)}\delta_{ij}p + \frac{\beta_s}{3}\delta_{ij}pT \\ \zeta = \frac{\alpha(1-2v)}{2G(1+v)}\sigma_{kk} + \frac{\alpha^2(1-2v)^2+(1+v_u)}{2G(1+v)(v_u-v)}p - \phi(\beta_f - \beta_s)T \end{cases}, \qquad \text{(S5)}$$

where ε_{ij} is the change of strain of the rock, σ_{ij} is the change of stress of the rock (tension positive), p, T and ζ are the change of pore pressure, temperature and pore volume, respectively. The rock property constants are as follows: α is *Biot*'s coefficient, v and v_u are the drained and undrained Poisson's ratios, G is the bulk shear modulus, B is Skempton's pore pressure coefficient, β_s and β_f are the volumetric thermal expansion

coefficient of the solid and the pore fluid, respectively. This theory was used to study the mechanical stability of geothermal reservoirs during cold water injection [*Simone*, 2013] and the role of thermo-poromechanical processes on reservoir seismicity and permeability enhancement [*Ghassemi & Tao*, 2016]. Recently, the fully coupled thermal-hydraulic-mechanical model and finite element model, which are similar to *McTigue's* theory, were presented for heat and gas transfer in thermal stimulation enhanced coal seam gas recovery [*Teng et al.*, 2018], and fractured geothermal reservoirs [*Salimzadeh et al.*, 2018], respectively.

Based on the above brief review about the thermoelasticity, poroelasticity and the coupling on the thermo-poroelasticity, we can found that all the prior researches focus on either the temperature field influences the stresses/strains [*Carlson*, 1973; *Wong and Brace*, 1979; *Nowacki*, 1986; *Wang et al.*, 1989; *Hetnarski and Eslami*, 2008], or stresses/strains influence the temperature field of thermoelastic solids [*Duhamel*, 1837; *Neumann*, 1885; *Biot*, 1956; *Lessen*, 1956; *Boley and Weiner*, 1960] and pore pressure of porous rocks [*Biot*, 1941; *Geertsma*, 1957a], respectively. But up to now, a clear understanding of the temperature response of fluid-saturated porous rocks to changes in stresses and strains has been lacking. It means that we know very little about how the stresses and strains influence the temperature field of the fluid-saturated rocks. Consequently, in this study, we try to derive the theoretical basis about the temperature response of fluid-saturated porous rocks to changes in stresses and strains during the adiabatic process, and then carry out systematic experiments under undrained and drained conditions.

Detailed descriptions about the measurements system

To measure β_{wet}, we improved the hydrostatic compression system used to measure β_{dry}. Figure S1 shows the improved system with two pressure vessels and a servo-controlled pump that provides a pressure of up to 130 MPa at room temperature. Both pressure vessels are filled with silicone oil as the pressure medium. To avoid oil permeating into the pores of the rock sample, there are two dielectric silicone and rubber end pieces, each 50 mm in height, at the top and bottom of the rock specimen. The silicone end piece includes two parts, each 25 mm thick (Figures S1, 3a and 4a). One is hard silicone. The other is soft silicone, which is made of two original silicone components produced by Shin-Etsu Chemical Co., Ltd.

All of the silicone and rubber end pieces are 50 mm in diameter, like the rock specimen. We enveloped them together with a rubber jacket and three O-rings on each end piece. One O-ring is between the hard silicone/rubber end piece and the rubber jacket. Two are around the outside of the rubber jacket (Figure 3a, 3e). We drilled a hole that was 2.8 mm in diameter (D_h) and 26.0 mm in depth (H) in the center of each rock specimen (Figures S1, 3 and 4). Then, we installed temperature sensors (PT1000 M213 Class-B, one kind of platinum resistance temperature detector produced by the Heraeus Sensor Technology GmbH, Kleinostheim, Germany) through the top silicone end piece in the center (T01) and on the surface (T02) of the sample in addition to a temperature sensor in the oil (T03) (Figures S1, 3 and 4). The three temperature sensors were connected to the temperature data logger, which we designed based on a bridge reversal excitation circuit with a high temperature resolution of ~1.0 mK at room temperature [*Qin et al.*, 2013]. There is a pressure transducer (PG-2TH, Kyowa electronic instruments, Co.Ltd, Tokyo, Japan) which is connected to a pressure data logger (TDS-303, Tokyo Sokki Kenkyujo Co. Ltd, Tokyo, Japan). The sampling intervals of temperature and pressure are 1 s. Thus, during the rapid loading and unloading processes, we can monitor the confining pressure (oil pressure, P) and temperature changes of the rock specimen and oil with the pressure and temperature data loggers with a data sampling interval of 1 s.

Detailed descriptions about the experimental procedure

To saturate the porous rock specimens, they were placed in a cup filled with ion-exchanged water, and then, they were placed in a vacuum chamber and vacuumed for more than 6 days. During this time, all of the air was removed from the pores, and the pores were saturated with water. For the quasi-undrained conditions, a steel tube with a miniature temperature sensor T01 was placed into the central hole in the specimen (Figures 3a–3c). For the quasi-drained conditions, only a miniature temperature sensor T01 was installed in the central hole (Figure 4). Then, the sample assembly was put together as shown in Figures 3 and 4 and was placed into Vessel B (Figure S1).

The new hydrostatic compression system, which was improved from a previous system for use in this study, was to accomplish the rapid loading and unloading (Figure S1). For the rapid loading experiments, there were three main steps: (1) valves V02 and V03 were closed, while valve V01 was left open (Figure S1); (2) the confining pressure in Vessel A was increased to a predetermined pressure (e.g., 125 MPa) using the servo-controlled pump, while the confining pressure in Vessel B was kept constant at a lower pressure (e.g., ~0–2 MPa) and at room temperature for at least 4 hours to allow the system to achieve thermal equilibrium; and (3) the rock specimen was rapidly loaded by manually opening valve V02. The confining pressures in Vessels A and B would immediately trend to the same value after valve V02 was opened.

For the rapid unloading, there are also three main steps: (1) valve V03 was closed, while valves V01 and V02 were kept open; (2) the confining pressures in Vessels A and B were increased to a predetermined pressure (e.g., 10 MPa) using the servo-controlled pump and were kept constant at room temperature for at least 4 hours to enable the system's temperature to reach equilibrium; and (3) valve V02 was manually closed, and valve V03 was opened to instantaneously unload the confining pressure in Vessel B to atmospheric pressure (~0.1 MPa). The key experimental records and results are presented in Table 3. In this study, the maximum confining pressure in Vessel B was set as ~15 MPa, which is much lower than the strength of the rocks, to prevent any influence of stress loading on the temperature response during multiple tests of the same rock specimen.

Thermal equilibrium between the skeletal framework and the pore fluid

Whether under undrained or drained conditions, the temperature change of the skeletal framework is distinct from that of the pore fluid at the initial moment of rapid loading/unloading, which is demonstrated by Equations (11) and (21) (i.e., $\Delta T_{\mathrm{frm}} \neq \Delta T_{\mathrm{f}}$). However, using Equations (13) and (26), we obtain the apparent temperature change of the fluid-saturated porous rock (ΔT) based on the fact that thermal equilibrium between the skeletal framework and pore fluid can be achieved within the data sampling interval (i.e., 1 s) after instantaneous loading/unloading. In this section, we investigate the thermal equilibrium using the estimated characteristic distance and numerical simulation.

1) Estimation of characteristic distance

Through dimensional analysis of the heat conduction equation, we can obtain the fact that if the temperature changes occur within a characteristic time interval τ, they will propagate a distance on the order of

$$l = \sqrt{k\tau}, \qquad \text{(S6)}$$

where κ is thermal diffusivity. Similarly, a time,

$$\tau = l^2/k, \qquad \text{(S7)}$$

is required for the temperature changes to propagate a distance l [*Turcotte and Schubert*, 2014]. Such a simple consideration can be used to obtain useful estimations of the thermal effects and the thermal equilibrium that occur in porous rocks during rapid loading/unloading processes.

There are currently around 4170 known mineral species. Among these minerals, approximately 50 are common rock-forming minerals. Silicates are the most abundant group of minerals. They constitute over 90% of the Earth's crust. The feldspar group represents about 60% of these crustal minerals, while silica (mainly quartz) represents 10% to 13% [*Demange*, 2012]. Table S2 lists the thermal properties of 52 common rock-forming minerals [*Pan*, 1993; *Schön*, 2011]. Pyrite has the greatest thermal diffusivity (κ_{pyrite} = 7.66 mm^2/s), while gypsum has the lowest thermal diffusivity (κ_{gypsum} = 0.51 mm^2/s). The main rock-forming minerals in the crust are quartz, orthoclase, plagioclase, mica, amphibole, pyroxene, olivine, and calcite [*Xiao et al.*, 2017]. Consequently, we estimated the characteristic distances for several main rock-forming minerals and water using Equation (S6) and the known thermal diffusivities

(Tables S2, S3). The thermal properties of rock-forming minerals and estimations of thermal characteristic time/distance are also stored and provided in Zenodo (http://doi.org/10.5281/zenodo.4242969). The results indicate that temperature changes can propagate 1.0–2.0 mm in most of the main rock-forming minerals within the data sampling interval of 1 s used in this study. Even if the thermal diffusivity is as low as those of gypsum (κ_{gypsum} = 0.51 mm^2/s) and water (κ_{water} = 0.15 mm^2/s), the characteristic distances (when τ' = 1 s) can reach up to 0.714 mm and 0.387 mm, respectively (Figure S2).

Generally, for most porous rocks in the crust, the sizes of the solid grains, i.e., rock-forming minerals, and pores are limited. Figure S2 shows photomicrographs of thin sections of fault rocks (cataclasite, breccia, and gouge) from the Longmenshan Fault Zone (a-b), the Chelungpu Fault Zones (c-d), the Rajasthan sandstone (RJS) from India (e), and a cross-section of micro-CT image of the Berea sandstone (BRS) from the U.S. (f). Except for the RJS and the BRS, most of the rocks used in this study were collected from the Longmenshan and Chelungpu Fault Zones (Table 2). Thus, the internal structures of the crustal rocks shown in Figure S2 have certain representativeness in this study. They indicate that the sizes of the solid grains in porous rocks are usually within ~1.0 mm, which are less than the characteristic distances for 1 s in most of the main rock-forming minerals. In addition, even if the porosity is up to 0.2, e.g., in the BRS (i.e., ϕ = 0.2), the sizes of the pores are usually less than 0.2 mm, which is about half of the characteristic distance for 1 s in water (l = 0.387 mm, Figure S2). In other words, the solid grains and pore water can approximately reach thermal equilibrium through heat conduction within 1 s after instantaneous loading/unloading.

2) Numerical simulation

Based on the above investigation on the sizes of the solid grains and pores in rocks, we modeled the internal structure of water-saturated rock, in which each solid grain is surrounded by pore water, and the sizes of the solid grains and pores are up to 1.0 mm and 0.3 mm, respectively (Figure S3a1). In this case, the equivalent porosity is up to 0.408 (i.e., ϕ = 0.408).

To have a clear understanding of the thermal equilibrium reached between the grains and the pore water, a heat conduction finite element model framed within a two-

dimensional Cartesian coordinate system (2d*xy*) was constructed. The heat conduction equation for the 2d*xy* system is

$$\begin{cases} (\rho c)\frac{\partial T}{\partial t} = \lambda\left(\frac{\partial^2 T}{\partial x^2} + \frac{\partial^2 T}{\partial y^2}\right) + A \\ A = \beta(\rho c)\frac{\partial P}{\partial t} \\ T(x, y, 0) = 0 \end{cases}, \qquad \text{(S8)}$$

Where λ is the thermal conductivity; (ρc) is the volumetric heat capacity; and β is the adiabatic pressure derivative of the temperature. A is the heat source term driven by the change in confining pressure during loading/unloading processes. The initial condition $T(x,y,0)$ is set as 0 since the entire rock specimen assembly achieves thermal equilibrium before loading/unloading (see the Detailed descriptions about the experimental procedure in supporting information).

Here, taking the following process as an example: the confining pressure increases from air pressure to 10 MPa within dt=0.001 s under undrained conditions (i.e., ΔP_c = 10 MPa), and Skempton's coefficient is considered to B = 0.5. According to Equation (9), the changes in the pore pressure (ΔP_f) and the effective pressure (ΔP^{eff}) can be calculated since the effective stress coefficient α can be estimated from the equivalent porosity (ϕ=0.408) using equation (28). The estimated α, the calculated ΔP^{eff} and ΔP_f are listed in Figure S3. After setting the β of the skeletal framework (β_{frm}) to 3.85 mK/MPa, which is the mean value of β for dry rocks [*Yang et al.*, 2017], we solved the temperature field evolution after rapid loading when the solid grains are gypsum, an average of the main rock-forming minerals (RFM), and α-quartz in models M-01, -02, and -03, respectively (Figure S3). The time step was 0.001 s in these models. The thermal properties of gypsum, RFM, α-quartz and water are listed in Table S3. Figure S3 shows the thermal equilibrium process between the grains and the pore water at t=0.001 s, 0.25 s, 0.5 s, and 1.0 s after rapid loading. First, taking model M-01 as an example, at the initial moment of rapid loading (t=0.001 s), the temperature increases 0.0202 K within the solid grains (gypsum), but 0.0884 K in the pore water (Figure S3a1). There is a still temperature difference between the grains and the pore water at t=0.25 s (Figure S3a2). However, the temperature difference becomes very small after 0.5 s (Figure S3a3). At t=1.0 s, both the temperature within grains and the pore water trend to 0.0569 K, which is the same as the final balance temperature T_{end} calculated by theoretical Equations (9)-(13) (Figure S3a4 and Table S4). It is worth noting that

gypsum has the lowest thermal diffusivity (κ_{gypsum}=0.51 mm^2/s) of the main RFMs (Table S2). This means that the thermal equilibrium time will be shorter than 1.0 s since the thermal diffusivity of the grains is higher than κ_{gypsum}. For example, in models M-02 and -03, the samples almost reach thermal equilibrium after 0.5 s (Figures S3b3 and S3c3) because the thermal diffusivities of the RFM and the α-quartz are up to 2.08 mm^2/s and 4.15 mm^2/s, respectively (Table S3). Figure S4 shows the temperature profiles along line *A*-*A*' (Figure S3a1) at *t*=0.001 s, 0.25 s, 0.5 s, 0.75 s, and 1.0 s. It also shows that 1.0 s is enough for the water-saturated rocks to achieve thermal equilibrium after the confining pressure changing. In addition, Movies S1, S2, and S3 (in the Supporting Information) provide very clear images and processes to understand the inner temperature evolution of the entire water-saturated rock specimen within 1.0 s after instantaneous loading. Movies S1, S2, and S3 are also deposited in Zenodo (http://doi.org/10.5281/zenodo.4242969).

From the above characteristic distance analysis and numerical simulation, the results reveal that water-saturated rocks can reach achieve thermal equilibrium within 1.0 s after the confining pressure changes.

Table S1. Temperature response of water-saturated Longmenshan limestone (L27) and Rajastan sandstone (RJS) to changes in confining pressure under drained/undrained conditions

Table S2. Thermal Properties of Rock-forming Minerals and Estimations of Characteristic Time/Distance

Movie S1. Internal temperature evolution of the water-saturated sample within 1 s after instantaneous loading in model M-01. Here the solid grains are set to be gypsum with κ_{Gypsum} = 0.51 mm^2/s. In the movie, "u", the title of the legend, means the temperature change (d*T*) with the unit of K. The temperature evolution starts from *t*=0 s (the time point of instantaneous loading) to t=1 s. The time step is 0.001 s. Thus there are a total of 1000 computational steps. It means at the "step 1", "step 500" and "step 1000" in the movie are *t*=0.001 s, *t*=0.5 s and *t*=1.0 s, respectively, after instantaneous loading.

"unoda0" is the name of the temperature field in the finite element model (similarly hereafter).

Movie S2. Internal temperature evolution of the water-saturated sample within 1 s after instantaneous loading in model M-02. Here the solid grains are set to be main rock-forming minerals averaged (RFM) with $\kappa_{\mathrm{RFM}} = 2.08\ \mathrm{mm}^2/\mathrm{s}$.

Movie S3. Internal temperature evolution of the water-saturated sample within 1 s after instantaneous loading in model M-03. Here the solid grains are set to be α-quartz with $\kappa_{\alpha\text{-quartz}} = 4.15\ \mathrm{mm}^2/\mathrm{s}$.

References

Biot, M. A. (1941), General Theory of Three‐Dimensional Consolidation, Journal of Applied Physics, 12(2), 155-164, doi:10.1063/1.1712886.

Biot, M. A. (1956), Thermoelasticity and Irreversible Thermodynamics, Journal of Applied Physics, 27(3), 240-253, doi:10.1063/1.1722351.

Carlson D.E. (1973) Linear Thermoelasticity. In: Truesdell C. (eds) Linear Theories of Elasticity and Thermoelasticity. Springer, Berlin, Heidelberg. https://doi.org/10.1007/978-3-662-39776-3_2.

De Simone, S., V. Vilarrasa, J. Carrera, A. Alcolea, and P. Meier (2013), Thermal coupling may control mechanical stability of geothermal reservoirs during cold water injection, Physics and Chemistry of the Earth, Parts A/B/C, 64, 117-126, doi:10.1016/j.pce.2013.01.001.

Demange, M. (2012), Mineralogy for petrologists : optics, chemistry, and occurrence of rock-forming minerals, edited, CRC Press, London, doi:10.1201/9780429355172.

Dong, H. (2008), Micro-CT imaging and pore network extraction, Ph.D. thesis, Imperial College London.

Duhamel JMC (1837), Second mémoire sur les phénomènes thermo-mécaniques Second memoir on thermo-mechanical phenomena, Journal de l'Ecole Polytechnique, Tome 15, Cahier 25, pp 1–57.

Geertsma J. (1957a), The effect of fluid Pressure decline on volumetric Changes of porous rocks，Petroleum Transactions, AIME, 210, 331-340.

Geertsma, J. (1957b), A remark on the analogy between thermoelasticity and the elasticity of saturated porous media, Journal of the Mechanics and Physics of Solids, 6(1), 13-16, doi: 10.1016/0022-5096(57)90042-X.

Ghassemi, A., and Q. Tao (2016), Thermo-poroelastic effects on reservoir seismicity and permeability change, Geothermics, 63, 210-224, doi: 10.1016/j.geothermics.2016.02.006.

Hashimoto, Y., K. Ujiie, A. Sakaguchi, and H. Tanaka (2007), Characteristics and implication of clay minerals in the northern and southern parts of the Chelung-pu fault, Taiwan, Tectonophysics, 443(3), 233-242.

Hetnarski, R. B., and M. R. Eslami (2008), Thermal Stresses—Advanced Theory and Applications (Solid Mechanics and Its Applications), Springer, Netherlands, doi:https://doi.org/10.1007/978-3-030-10436-8.

Lessen, M. (1956), Thermoelasticity and thermal shock, Journal of the Mechanics and Physics of Solids, 5(1), 57-61, doi:https://doi.org/10.1016/0022-5096(56)90007-2.

Lide, D. R. (2010), CRC handbook of chemistry and physics, 90th Edition (CD-ROM Version 2010), CRC press/Taylor and Francis, Boca Raton, Fla.

McTigue, D. (1986), Thermoelastic response of fluid‐saturated porous rock, Journal of Geophysical Research: Solid Earth (1978–2012), 91(B9), 9533-9542.

McTigue, D. F. (1990), Flow to a heated borehole in porous, thermoelastic rock: Analysis, Water Resources Research, 26(8), 1763-1774, doi:10.1029/WR026i008p01763.

Neumann F (1885), Vorlesung über die Theorie des Elasticität der festen Körper und des Lichtäthers. Teubner, Leipzig (Meyer, Breslau).

Norris, A. (1992), On the correspondence between poroelasticity and thermoelasticity, Journal of Applied Physics, 71(3), 1138-1141, doi:10.1063/1.351278.

Nowacki, W. (1986), Thermoelasticity, 2nd ed., PWN-Polish Scientific Publishers, Warsaw, and Pergamon Press, Oxford, doi:10.1016/C2013-0-03247-1.

Pan, Z. (1993), Crystallography and mineralogy, 3rd Edition [in Chinese], Geological Publishing House, Beijing.

Qin, Y., X. Yang, B. Wu, Z. Sun, and X. Shi (2013), High resolution temperature measurement technique for measuring marine heat flow, Sci. China Technol. Sci., 56(7), 1773-1778, doi:10.1007/s11431-013-5239-9.

Salimzadeh, S., A. Paluszny, H. M. Nick, and R. W. Zimmerman (2018), A three-dimensional coupled thermo-hydro-mechanical model for deformable fractured geothermal systems, Geothermics, 71, 212-224, doi:10.1016/j.geothermics.2017.09.012.

Schön, J. H. (2011), Physical properties of rocks: a workbook, Elsevier, Oxford.

Teng, T., Y. Zhao, F. Gao, J. G. Wang, and W. Wang (2018), A fully coupled thermo-hydro-mechanical model for heat and gas transfer in thermal stimulation enhanced coal seam gas recovery, International Journal of Heat and Mass Transfer, 125, 866-875, doi:10.1016/j.ijheatmasstransfer.2018.04.112.

Turcotte, D., and G. Schubert (2014), Geodynamics, 3rd ed., Cambridge University Press, Cambridge, U. K.

Wang, H. F., B. P. Bonner, S. R. Carlson, B. J. Kowalls, and H. C. Heard (1989), Thermal stress cracking in granite, Journal of Geophysical Research, 94(B2), 1745-1758.

Wang, H., H. Li, J. Si, Z. Sun, and Y. Huang (2014), Internal structure of the Wenchuan earthquake fault zone, revealed by surface outcrop and WFSD-1 drilling core investigation, Tectonophysics, 619–620, 101-114, doi:10.1016/j.tecto.2013.08.029.

Wong, T.-f., and W. Brace (1979), Thermal expansion of rocks: some measurements at high pressure, Tectonophysics, 57(2), 95-117.

Xiao, Y., R. Zheng, and J. Deng (2017), Petrology introduction, 4th Edition [in Chinese], Geological Publishing House, Beijing.

Yang, X., W. Lin, O. Tadai, X. Zeng, C. Yu, E.-C. Yeh, H. Li, and H. Wang (2017), Experimental and numerical investigation of the temperature response to stress changes of rocks, *Journal of Geophysical Research: Solid Earth*, *122*(7), 5101-5117, doi:10.1002/2016JB013645.

Zimmerman, R. W. (2000), Coupling in poroelasticity and thermoelasticity, International Journal of Rock Mechanics and Mining Sciences, 37(1), 79-87, doi: 10.1016/S1365-1609(99)00094-5.